Journal of Nuclear Medicine, published on January 26, 2017 as doi:10.2967/jnumed.116.183343

PET/MR Imaging in the Presence of Metal Implants: Completion of the Attenuation Map from PET Emission Data.

Niccolo Fuin[1], Stefano Pedemonte[1], Onofrio A Catalano[1], David Izquierdo-Garcia[1], Andrea Soricelli[2,3], Marco Salvatore[2], Keith Heberlein[4], Jacob M Hooker[1], Koen Van Leemput[1,5] and Ciprian Catana[1].

[1] Athinoula A. Martinos Center for Biomedical Imaging, Department of Radiology, Massachusetts General Hospital and Harvard Medical School, Charlestown, MA, USA.

[2] SDN - Istituto di Ricerca Diagnostica e Nucleare, IRCCS, Naples, Italy.

[3] University of Naples Parthenope, Department of Motor Sciences and Healthiness, Naples, Italy.

[4] Siemens Medical Solutions USA, MR RD Collaborations, Charlestown, MA, USA.

[5] Technical University of Denmark, Department of Applied Mathematics and Computer Science, Lyngby, Denmark.

Corresponding author:

Niccolo Fuin
149 13th St, Charlestown, MA 02129
Athinoula A. Martinos Center for Biomedical Imaging
Massachusetts General Hospital and Harvard Medical School
E-mail: nfuin@mgh.harvard.edu

Short title: PET/MR Implants Attenuation Correction

Word count: 4910

Financial Support: Funding for this work was provided by NIH grant 1R01EB014894 and DOE training grant DE-SC0008430.

ABSTRACT

We present a novel technique for accurate whole body attenuation correction (AC) in the presence of metallic endoprosthesis, on integrated non-time-of-flight (non-TOF) PET/MR imaging scanners. The proposed implant PET-based attenuation map completion (IPAC) method performs a joint reconstruction of radioactivity and attenuation from the emission data to determine the position, shape and linear attenuation coefficient (LAC) of metallic implants.

Methods

The initial estimate of the attenuation map is obtained using the MR Dixon-method currently available on the Siemens Biograph mMR scanner. The attenuation coefficients in the area of the MR image subjected to metal susceptibility artifacts are then reconstructed from the PET emission data using the IPAC algorithm. The method was tested on eleven subjects presenting thirteen different metallic implants, who underwent CT and PET/MR scans. Relative mean LACs and Dice Similarity Coefficients (DSCs) were calculated in order to determine the accuracy of the reconstructed attenuation values and the shape of the metal implant, respectively. The reconstructed PET images were compared to those obtained using the reference CT-based approach and the Dixon-based method. aRC images were generated in each case and voxel-based analyses were performed.

Results

The error in implant LAC estimation, using the proposed IPAC algorithm, was 15.7±7.8%, which was significantly smaller than the Dixon- (100%) and CT- (39%) derived values. A

mean DSC of 73±9% was obtained when comparing the IPAC- to the CT-derived implant shape. The voxel-based analysis of the reconstructed PET images revealed quantification errors (aRC) of 13.2±22.1% for the IPAC- with respect to CT-corrected images. The Dixon-based method performed substantially worse with a mean aRC of 23.1±38.4%.

Conclusion: We have presented a non-TOF emission-based approach for estimating the attenuation map in the presence of metallic implants, to be used for whole body AC in integrated PET/MR scanners. The Graphics Processing Unit implementation of the algorithm will be included in the open-source reconstruction toolbox Occiput.io.

Keywords: metal implant, integrated PET/MR, attenuation correction, MLAA.

INTRODUCTION

Accurate estimation of photon attenuation is one of the primary challenges in achieving unbiased measurements of the radiotracer concentration in hybrid positron emission tomography / magnetic resonance (PET/MR) imaging (*1*). Current PET/MR scanners are not equipped with a transmission source (*2,3*) or X-Ray Computed Tomography (CT) components. Thus, the 511 keV photon attenuation maps (μ-maps) need to be estimated directly from the MR and/or PET data. While substantial progress in generating accurate head MR-based μ-maps has been made (*4-9*), there are still many hurdles in estimating whole body μ-maps (e.g. bone tissue misclassification, arm truncation due to the limited transaxial MR field of view, susceptibility artifacts caused by foreign objects, etc.) (*10*). In this manuscript, we propose a method to correct for the errors in the PET images arising from MR susceptibility artifacts (e.g. image distortions and signal voids) around metallic objects (e.g. prosthetic devices) (*11*).

In PET/CT imaging, metallic objects lead to streak artefacts in the reconstructed CT images, diminishing their quality and biasing the PET images reconstructed using CT-based μ-maps. In PET/MR imaging, MR susceptibility artifacts that extend well beyond the implant, propagate as signal voids in the resulting MR-based μ-maps. Additionally, the implant attenuation itself is completely ignored. These two effects lead to substantial bias in PET quantification both locally and globally, and can potentially compromise the clinical interpretability of the resulting PET images. We propose here a novel IPAC method to minimize the bias due to metallic objects in PET quantification.

AC strategies proposed for PET/MR can be grouped broadly into three categories: approaches based on MR segmentation, methods based on MR-CT atlases, and techniques aimed at jointly estimating activity and attenuation from PET emission data. While the first two categories have been shown to achieve promising results for attenuation estimation of human tissues, they cannot account for the presence of metallic implants. For example, the segmentation-based method available on the Biograph mMR (Siemens Healthcare, Erlangen, Germany) (*12*) classifies metal implants and the surrounding tissue as air. This, in turns, propagates a large bias into the emission image. In atlas-based methods, μ-map image estimates are generated through a propagation scheme by locally matching a subject's MR-derived morphology to an MR-CT template set using local image similarity measurements (*4-6*). An MR-CT atlas-based attenuation synthesis method (*13*) has been adapted in (*14*) to include metal artifact correction. However, given the high degree of variability in the position and shape of metal implants, and the large deformations of the MR images in the adjacent areas, current methods based on atlases are of limited applicability. Creating databases large enough to account for the wide range (i.e. shape, dimension, composition) of metallic implants is problematic; incomplete MR data and deformations are complicating the required intra- and inter-subject registrations of the training datasets.

Methods to simultaneously reconstruct the radioactivity and attenuation have previously been proposed (*15-22*). A particularly influential approach is referred to as Maximum-Likelihood reconstruction of Attenuation and Activity (MLAA) (*15*). However, estimating the complete μ-map from the emission data is an ill-posed problem and the

resulting activity/attenuation pair often suffers from cross-talk artifacts, where bias in radioactivity features propagates into compensatory bias in the μ-map (and vice-versa), reflecting the non-uniqueness of the solution. The incorporation of time-of-flight (TOF) information has been demonstrated to reduce (but not to eliminate) the cross-talk effect (*16-20*) and the metal induced artifacts (*21*). TOF information is however currently unavailable on most of the installed hybrid PET/MR scanners.

In the case of the μ-maps generated from the MR data in the presence of an implant, information about the LACs is available everywhere except in the signal void region. Estimating only the missing data in this scenario is a less ill-posed problem than simultaneously estimating the entire μ-map (and the activity distribution) from the attenuated emission data.

Building on previous work published by Nuyts et al. (*15*), we describe a method for accurate determination of the position, shape and LAC of a metallic implant. In the standard Maximum-Likelihood reconstruction of Attenuation and Activity algorithm (*15*), the activity and μ-map update steps are alternatively performed using a gradient descent optimization method that does not directly enforce constraints. Moreover, in order to reach convergence, a different number of gradient ascent steps for the activity with respect to the μ-map must be used while iterating (or a relaxation coefficient must be added to the μ-map update formula).

For our purpose, we implemented the joint reconstruction using a Limited-memory BFGS quasi-Newton optimizer (L-BFGS-B) that permits the direct imposition of

constraints on the μ-map during reconstruction and does not require the predetermination of a relaxation coefficient.

We have applied the IPAC algorithm to phantom and human data acquired on the Biograph mMR scanner at two different institutions. The performance of the method was compared to both the AC method provided by the manufacturer (the Dixon-based approach) and the gold standard CT-based AC.

MATERIALS AND METHODS

Data Acquisition

In a phantom experiment, a hip cobalt/chromium endoprosthesis (LAC = 0.72 cm^{-1}) was placed in the center of a polymethyl methacrylate 16×16×30 cm^3 container (Supplemental Fig. 1). The phantom was filled with water mixed with ~54 MBq of ^{18}F-FDG and emission data were acquired for 5 minutes.

PET/MR datasets from 11 subjects presenting 13 different metal implants were included in the study. PET and MR data were acquired simultaneously using the Biograph mMR scanners installed at two of the authors' institutions (Table 1) as part of larger prospective studies approved by the respective institutional review boards. The emission data were acquired 205±67 minutes (mean ± standard deviation) after administration of 498±181 MBq (6.55 MBq/kg) of ^{18}F-FDG. The metal implants included one hip chromium alloy replacement, six hip titanium replacements, one femur replacement, three sets of titanium spine screws and two sets of dental implants (Table 1). The LAC of the implants were 0.36 cm^{-1} for titanium and 0.72 cm^{-1} for cobalt/chromium alloy. The implant characteristics and their material properties were obtained from the manufacturer

specifications. Data acquisition parameters, implant material and dimension specifications for each patient are presented in (Table 1 and Supplemental Table 1).

Emission data were acquired in 3D mode for 7.3±2.7 minutes per bed position and reconstructed using the standard 3D Ordinary Poisson Ordered-Subset Expectation Maximization Algorithm provided by the manufacturer with 3 iterations and 21 subsets (including corrections for random coincidences, variable detector sensitivity, dead-time, isotope decay, scatter and photon attenuation). Images were reconstructed into a 344×344×127 matrix with voxel sizes of 2.086×2.086×2.031 mm^3. MR data were acquired simultaneously with the PET data using a dual echo Dixon-VIBE sequence. All subjects underwent a low dose CT examination within one week of their PET-MR imaging scan using either a Siemens Biograph-64 or a Philips Gemini TF PET/CT scanner.

Joint Reconstruction of Activity and Attenuation

Building on previous work for non-TOF emission data (*22*), the simultaneous estimation of the activity and attenuation coefficients was here studied in the framework of maximum a posteriori estimation. The algorithm presented jointly estimates the vector of emission rates (λ) and the vector of LACs (μ) by maximization of the Poisson log-likelihood of emission data and regularization terms:

Equation 1

$$\hat{\lambda}, \hat{\mu} = \arg_{\lambda \geq 0} \min_{0.08 \leq \mu \leq 1} \left[\sum_d \left(c_d a_d \sum_i h_{id} \lambda_i + s_d + r_d \right. \right.$$

$$\left. \left. - \nu_d \log \left(c_d a_d \sum_i h_{id} \lambda_i + s_d + r_d \right) \right) \right] - \alpha \log p(\lambda) - \beta \log p(\mu),$$

where the elements h_{id} represent the geometric probability that photons emitted from voxel i are detected in line of response d; ν_d are the emission data; $a_d = exp(\sum_i \mu_i l_{id})$ are the attenuation factors; c_d are the detector normalization factors; l_{id} is the intersection length of the line of response d with voxel i; s_d and r_d are the expected contributions of scatter and random coincidences respectively. The space-invariant smoothing priors for λ and μ, used for regularization, are of the form: $\log p(x) = \frac{1}{4} \sum_i \sum_k w_{ik} (x_i - x_k)^2$; with $w_{ik}=1$ when pixels i, k are neighbors and $w_{jk}=0$ otherwise. Each voxel i is connected to its 26 nearest neighbors. Variables α and β are the regularization parameters.

The joint optimization was implemented using a L-BFGS-B algorithm (*23*). The BFGS is a quasi-Newton method, which uses an approximation of the inverse Hessian matrix to steer its search. The Hessian matrix is approximated from successive gradient values, so only the computation of the gradients is necessary for the optimization. The gradients of the cost function in Equation 1 with respect to λ and μ are given by the following equations:

Equation 2

$$\nabla_{\lambda_i} = \frac{\lambda_i}{\sum_d h_{id} c_d a_d} \left(\sum_d h_{id} c_d a_d - \sum_d h_{id} \frac{v_d}{\sum_j h_{jd} \lambda_j \frac{s_d}{a_d} \frac{r_d}{a_d c_d}} \right) - \alpha \nabla_{\lambda_i} \log p(\lambda)$$

Equation 3

$$\nabla_{\mu_i} = 1 - \frac{\sum_d h_{id} c_d v_d}{\sum_d h_{id} \left(r_d + s_d a_d + a_d c_d \sum_j h_{jd} \lambda_j \right)} + \beta \nabla_{\mu_i} \log p(\mu)$$

The gradients of the smoothing prior term is computed by applying the Laplace filter to λ and μ respectively. The "L" in L-BFGS stands for limited memory (*23*), since the algorithm maintains a history of the past $m = 16$ updates of the gradients to estimate the Hessian and its inverse. The step length in the minimization of the log-posterior is defined implicitly, therefore eliminating the need for the predetermination of a relaxation coefficient. Since the choice of the initial inverse Hessian approximation has demonstrated to be critical, the algorithm was here initialized with an estimation obtained after 2 iterations of the standard gradient ascent Maximum-Likelihood reconstruction of Attenuation and Activity algorithm. Finally, the L-BFGS-B is a box-constrained solver that permits the imposition of non-negativity constraints and explicit constraints in the estimation of the μ-map.

The μ-maps used for the algorithm initialization were generated using the method currently available on the Biograph mMR scanner (*12*). The images acquired with the Dixon-VIBE sequence are segmented into 3 tissue classes: air, fat and soft tissue. LACs of 0, 0.085 and 0.0968 cm^{-1} were then assigned to these tissue classes, respectively. A semi-automatic inpainting method similar to (*24*) was used to segment the region of MR void

produced by metal susceptibility artifacts (MSA). A LAC of 0.0968 cm^{-1} was assigned to this region as an initialization value.

During reconstruction, the Dixon μ-map values were held fixed in the region outside the MSA void; utilizing the box constraint feature of L-BFGS-B, the LACs inside the void were constrained between 0.08 and 1 cm^{-1}, and non-negativity constraints were applied to the λ coefficients ($\lambda_i \geq 0$). An isotropic quadratic prior with a small weight α=0.02, β = 0.01 was included in the radioactivity and attenuation update functions. Reconstructed μ-maps, obtained with the algorithm described above, will be denoted as IPAC μ-maps henceforth.

Scatter distribution sinograms were calculated using a fully 3D implementation of the single scatter simulation method (*25*) with relative scaling, provided by the manufacturer. The whole scatter correction process went through two iterations (using the first μ-map estimation as the input for the second iteration) in order to refine the scatter estimate.

CT-AC μ-Map Generation

To compare the proposed IPAC method to CT-based AC, the CT images were converted from Hounsfield Units (HU) to LACs (μ_{CT}) at 511 KeV using the bilinear transformation method described in (*26*). Gaussian smoothing with a 4 mm kernel was applied to these μ-maps to match the PET spatial resolution. The resulting reference CT μ-maps were rigidly registered to the corresponding IPAC μ-maps inside the MSA void and non-rigidly registered (using Elastix software (*27*)) outside the void. Non-rigid registration

outside the void is desirable since CT and MR images were acquired at different times with the patient's hip in different positions with respect to the pelvis.

Due to saturation of the HU dynamic range in clinical CT, an incorrect LAC of 0.24 was assigned to the metal implant region when applying the standard transformation method described in (*26*). Additionally, CT μ-maps were reconstructed using the standard reconstruction algorithm implemented in the scanner and therefore presented metal induced artifacts (techniques for the suppression of beam-hardening artifacts (*28*) were not applied). In order to limit the effect of these artifacts, the CT μ-map values outside the void but within the body contour and with LAC < 0.085 were set to 0.085 to generate thresholded CT (thCT) μ-maps.

Analysis of Image Quality

The accuracy in estimating the shape of the implant was evaluated by calculation of the DSC of the segmented IPAC μ-map with respect to the segmented thCT reference μ-map. In both μ-maps, every voxel with LAC > 0.2 cm^{-1} was considered to be part of the implant class. The accuracy in estimating the LAC of the metal compound was evaluated by calculation of the relative mean of the implant LACs and comparing it to the value obtained based on the characteristics of the respective metal implant.

AC factors in sinogram space generated from the IPAC, Dixon and thCT μ-maps were used to model attenuation during reconstruction with the Ordinary Poisson Ordered-Subset Expectation Maximization algorithm and the corresponding PET_{IPAC}, PET_{thCT}, and PET_{Dixon} volumes for all subjects were generated. Voxel-based analysis was performed to assess the accuracy of the μ-maps and reconstructed PET images. Only voxels included in

the body contour mask were used in these comparisons. Bland-Altman plots, bias, standard deviation and Pearson's coefficients were used to calculate the correlation of the PET_{IPAC} images with respect to the PET_{thCT} and PET_{Dixon} images. aRC were defined as follows:

Equation 4

$$aRC = \left|I_{Ref} - I_X\right| / I_{Ref}$$

where I_X corresponds to either the PET images (PET_{Dixon} or PET_{IPAC}) , and I_{ref} corresponds to the reference image PET_{thCT}.

RESULTS

In (Fig. 1) we present the CT μ-map and IPAC μ-map (Fig. 1) for the uniform ^{18}F-FDG phantom with a cobalt-chromium alloy implant (Supplemental Fig. 1). The shape of the implant was estimated in great detail using the IPAC algorithm (with conceivably better results than the CT). From (Fig. 1B) it can be also noted that saturation of the HU dynamic range leads to a truncation of the implant LACs in the CT image, whereas the correct implant LAC was obtained using the proposed method. The corresponding reconstructed PET images corrected with the CT- and IPAC-based AC methods are shown in (Supplemental Fig. 2).

Representative Dixon, CT and IPAC μ-maps are shown in Figures 2 and 3 and Supplemental Figures 3 and 4 for patients with right hip cobalt-chromium alloy endoprosthesis (Fig. 2), a titanium spinal pedicle screw implant (Fig. 3), titanium endoprosthesis on both hips (Supplemental Fig. 3) and dental implants (Supplemental Fig. 4). These images demonstrate excellent correspondence between the μ_{IPAC} and μ_{CT} maps, and the obvious misclassification of the tissues within the MSA void in the μ_{Dixon} map.

The implant LAC means and the DSCs for all eleven test subjects are given in Table 1. The mean LAC percentage error obtained with the IPAC method was 15.7 ± 7.8 %, which was significantly smaller than the Dixon- (100 %) and CT- (39 %) derived values. A mean DSC of 73 ± 9 % was obtained when comparing the IPAC- to the CT-derived implant shape. These results suggest that the proposed IPAC algorithm is capable of accurately reconstructing the shape and LAC of a metallic implant.

The reconstructed PET images corrected with the three AC methods for the subject shown in Figure 2 are presented in Figure 4. As expected, the largest errors occurred in the MSA void region. The results of the quantitative voxel-based analyses for all the subjects are summarized in Supplemental Table 1. The mean aRC was 13.2 ± 22.1% for the PET_{IPAC} and 23.1 ± 38.4% for the PET_{Dixon} across the whole field of view. The mean aRC in the MSA region around the implant was 20.3 ± 23.1% for the PET_{IPAC} and 80.1 ± 27.1% for the $PET_{Dixon.}$

Figure 5 shows the Bland-Altman plots for the voxel-based analyses for all the validation subjects, comparing the PET_{Dixon} (Fig. 4A) and the PET_{IPAC} (Fig. 4C) to the PET_{thCT} (Fig. 4B). Pearson's correlation coefficients were R_{IPAC} = 0.08 and R_{Dixon} = 0.33. The mean difference in all voxels, with respect to the PET_{thCT}, was 0.055 ± 0.56 for the PET_{IPAC} and 0.087 ± 0.91 for the PET_{Dixon}, demonstrating that the presented method significantly improves PET quantification in the presence of metal implants.

DISCUSSION

We have presented a method to estimate the location, shape and LAC of a metallic implant from non-TOF PET emission data in order to substantially improve the accuracy of the MR-based whole body μ-map estimation on integrated PET/MR scanners.

Our method relies on the assumptions that the metal implant have zero activity and a LAC higher than that of any body tissue. This establishes a special case where the estimation of the μ-map directly from the PET emission data is a less ill-posed problem. The proposed IPAC algorithm produces good results in patients presenting metal replacements in one or both hips (Supplemental Fig. 3) and composed of different materials. The method is also capable of reconstructing the shape of smaller metallic implants such as titanium pedicle screws and dental implants (Fig. 3 and Supplemental Fig. 4).

Overall, we would expect the performance of the proposed IPAC algorithm to depend on: the count statistics of the emission data; the spatial distribution of the radiotracer in the body to support μ-map estimation (which in turn depends on the type of radiotracer); the size of the MSA void, since sufficient information about the LACs is required to obtain a scaled solution (*20*); and the shape and dimensions of the metal implant. However, assessing the exact contribution of each of these factors was beyond the goal of this proof-of-concept study. Additionally, further investigation is required to assess the robustness of the method in other scenarios. In particular, the data used in this study were acquired approximately 3 hours after injection of ^{18}F-FDG while clinical whole body scans are typically performed 1 hour after injection, when the count statistics and contrast-to-noise ratios are different. Moreover, the performances of the IPAC method was not

evaluated for radiotracers other than ^{18}F-FDG. Finally, distinguishing between bone and soft tissue in the MSA void region is not possible with the current implementation.

The IPAC algorithm can be combined with other approaches for addressing the remaining issues in MR-based AC. The initial μ-map outside the void could be generated using an atlas-based method that properly accounts for bone tissue. Additionally, MR metal artifact reduction sequences (*29,30*) are expected to further improve the initial μ-map inside the void. For example, a slice encoding for metal artifact correction (SEMAC) sequence (*29*) has been proposed for reducing artifacts arising from hip arthroplasty. Using multiacquisition variable-resonance image combination (MAVRIC-SL), a similar sequence, the overall mean artifact area was reduced by 60% using 3-T MR in patients with hip arthroplasty (*30*). Although these sequences will not allow the estimation of the exact shape or LACs of the metal implants, they will further aid the joint-reconstruction, by minimizing the signal void and providing more accurate information about the tissue surrounding the implants. Alternatively, when the implant material is known so that its LAC can be obtained, the IPAC method could be used to precisely estimate the implant shape and location in the body. We also expect that TOF information, when available, could further improve the accuracy of the IPAC method in distinguishing between bone and soft tissue.

A package containing the necessary software will be included in the Graphics Processing Unit-based Occiput reconstruction toolbox (occiput.io, (*31*)) and its specific implementation for the Biograph mMR will be provided to interested users upon request.

CONCLUSION

We have presented an emission based approach for deriving the location, shape and LAC of metallic implants from non-TOF PET emission data. The IPAC algorithm can, in principle, be used in any PET/MR scanner. The results presented suggest that our method provides more accurate quantification than previously proposed MR-AC methods in the presence of metal implants, both in terms of the accuracy of the μ-maps and the PET quantification.

ACKNOWLEDGMENTS

Funding for this work was provided by NIH grant 1R01EB014894 and DOE training grant DE-SC0008430. We thank Dr. Edward K. Rodriguez from Orthopedic Trauma BIDMC and HMS for providing the hip implant endoprosthesis that was used in the phantom experiment.

REFERENCES

1. Catana C, Guimaraes AR, Rosen BR. PET and MR imaging: the odd couple or a match made in heaven? *J Nucl Med.* 2013;54:815–824.

2. Mollet P, Keereman V, Vandenberghe S, et al. Improvement of attenuation correction in time-of-flight PET/MR imaging with a positron-emitting source. *J Nucl Med*. 2014;55:329–336.

3. Bowen SL, Fuin N, Levine MA, Ciprian Catana. Transmission imaging for integrated PET-MR systems. *Phys Med Biol.* 2016;61:5547–5568.

4. Izquierdo–Garcia D, Hansen AE, Forster S, et al. An SPM8-based approach for attenuation correction combining segmentation and nonrigid template formation: application to simultaneous PET/MR brain imaging. *J Nucl Med.* 2014;55:1825–1830.

5. Torrado-Carvajal A, Herraiz JL, Malpica N, et al. Fast patch-based pseudo-CT synthesis from T1-weighted MR images for PET/MR attenuation correction in brain studies. *J Nucl Med*. 2016;57:136–143.

6. Burgos N, Cardoso MJ, Thielemans K, et al. Attenuation correction synthesis for hybrid PET-MR scanners: application to brain studies. *IEEE Trans Med Imaging.* 2014;33:2332–2341.

7. Keereman V, Fierens Y, Vandenberghe S, et al. MRI-based attenuation correction for PET/MRI using ultrashort echo time sequences. *J Nucl Med.* 2010;51:812–818.

8. Catana C, van der Kouwe A, Sorensen AG, et al. Towards implementing an MR-based PET attenuation correction method for neurological studies on the MR-PET brain prototype. *J Nucl Med.* 2010;51:1431–1438.

9. Mehranian A, Arabi H, Zaidi H. Quantitative analysis of MRI-guided attenuation correction techniques in time-of-flight brain PET/MRI. *Neuroimage*. 2016;15:123–133.

10. Izquierdo–Garcia D, Sawiak SJ, Knesaurek K, et al. Comparison of MR-based attenuation correction and CT-based attenuation correction of whole-body PET/MR imaging. *Eur J Nucl Med Mol Imaging.* 2014;41:1574–1584.

11. Hargreaves BA, Worters PW, Pauly KB, et al. Metal-induced artifacts in MRI. *AJR Am J Roentgenol.* 2011;197:547–555.

12. Martinez–Moller A, Souvatzoglou M, Delso G, et al. Tissue classification as a potential approach for attenuation correction in whole-body PET/MRI: evaluation with PET/CT data. *J Nucl Med.* 2009;50:520–526.

13. Hofmann M, Steinke F, Scheel V, et al. MRI-based attenuation correction for PET/MRI: a novel approach combining pattern recognition and atlas registration. *J Nucl Med.* 2008;49:1875–1883.

14. Bezrukov I, Schmidt H, Mantlik F, et al. MR-based attenuation correction methods for improved PET quantification in lesions within bone and susceptibility artifact regions. *J Nucl Med*. 2013;54:1768–1774.

15. Nuyts J, Dupont P, Stroobants S, et al. Simultaneous maximum a posteriori reconstruction of attenuation and activity distributions from emission sinograms. *IEEE Trans Med Imag.* 1999;18:393–403.

16. Salomon A, Goedicke A, Schweizer B, et al. Simultaneous reconstruction of activity and attenuation for PET/MR. *IEEE Trans Med Imag.* 2011;30:804–813.

17. Rezaei A, Defrise M, Bal G, et al. Simultaneous reconstruction of activity and attenuation in time-of-flight PET. *IEEE Trans Med Imag.* 2012;31:2224–2233.

18. Mehranian A, Zaidi H. Joint estimation of activity and attenuation in whole-body TOF PET/MRI using constrained Gaussian mixture models. *IEEE Trans Med Imag.* 2015;34:1808–1821.

19. Mehranian A, Zaidi H. Impact of time-of-flight PET on quantification errors in MR imaging-based attenuation correction. *J Nucl Med*. 2015;56:635–641.

20. Defrise M, Rezaei A, Nuyts J. Time-of-flight PET data determine the attenuation sinogram up to a constant. *Phys Med Biol.* 2012;57:885–899.

21. Davison H, ter Voert EE, Delso G, et al. Incorporation of time-of-flight information reduces metal artifacts in simultaneous positron emission tomography/magnetic resonance imaging. A simulation study. *Invest Radiol.* 2015;50:423–429.

22. Nuyts J, Bal G, Kehren F, et al. Completion of a truncated attenuation image from the attenuated PET emission data. *IEEE Trans Med Imag.* 2013;32:237–246.

23. Byrd RH, Lu P, Zhu C, et al. A limited memory algorithm for bound constrained optimization. *SIAM J Sci Comput*. 1995;16:1190–1208.

24. Ladefoged CN, Andersen FL, Beyer T et al. PET/MR imaging of the pelvis in the presence of endoprostheses: reducing image artifacts and increasing accuracy through inpainting. *Eur J Nucl Med Mol Imaging.* 2013;40:594–601.

25. Watson CC. New, faster, image-based scatter correction for 3D PET. *IEEE Trans Nucl Sci.* 2000;47:1587–1594.

26. Burger CL, Goerres G, Von Schulthess GK, et al. PET attenuation coefficients from CT images: experimental evaluation of the transformation of CT into PET 511-keV attenuation coefficients. *Eur J Nucl Med Mol Imaging*. 2002;29:922–927.

27. Klein S, Staring M, Pluim JPW, et al. Elastix: A toolbox for intensity based medical image registration. *IEEE Trans Med Imaging.* 2010;1:196–205.

28. Lemmens C, Faul D, Nuyts J. Suppression of metal artifacts in CT using a reconstruction procedure that combines MAP and projection completion. *IEEE Trans Med Imaging. 2009;28:250–260.*

29. Lu W, Pauly KB, Gold GE, et al. SEMAC: slice encoding for metal artifact correction in MRI. *Magn Reson Medicine.* 2009;62:66–76.

30. Choi SJ, Koch KM, Hargreaves BA, et al. Metal artifact reduction with MAVRIC SL at 3T MRI in patients with hip arthroplasty. *AJR Am J Roentgenol*. 2015;204:140–147.

31. Pedemonte S, Fuin N. Occiput.io (accessed October 30, 2016).

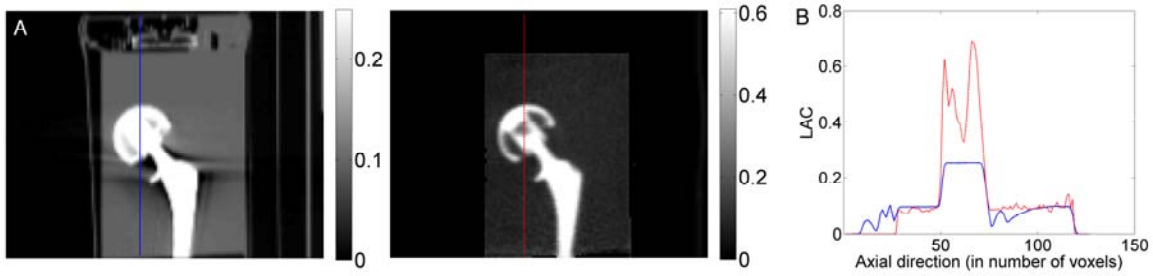

Figure 1

Uniform ^{18}F-FDG phantom with cobalt-chromium alloy implant. CT μ-map (A-left) and IPAC μ-map (A-right) are shown. The corresponding LAC profiles are shown in Figure B (CT μ-map in blue and IPAC μ-map in red).

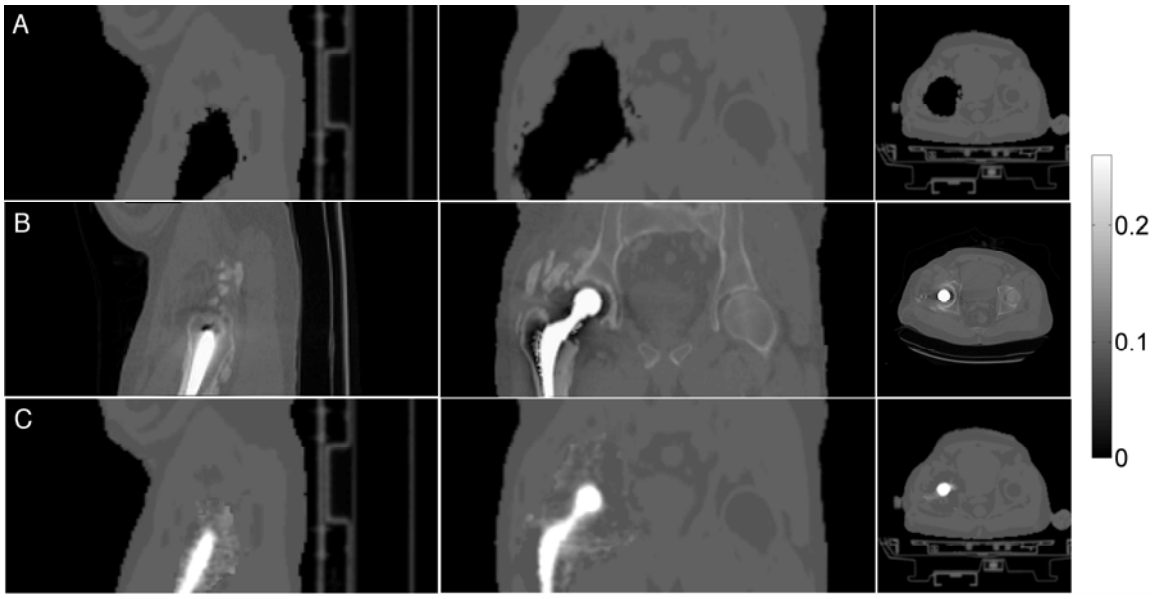

Figure 2

Patient presenting right hip cobalt-chromium alloy endoprosthesis (Patient 1). Dixon (A), CT (B) and IPAC (C) μ-maps are shown. The three columns show (from left to right) sagittal, coronal and axial planes.

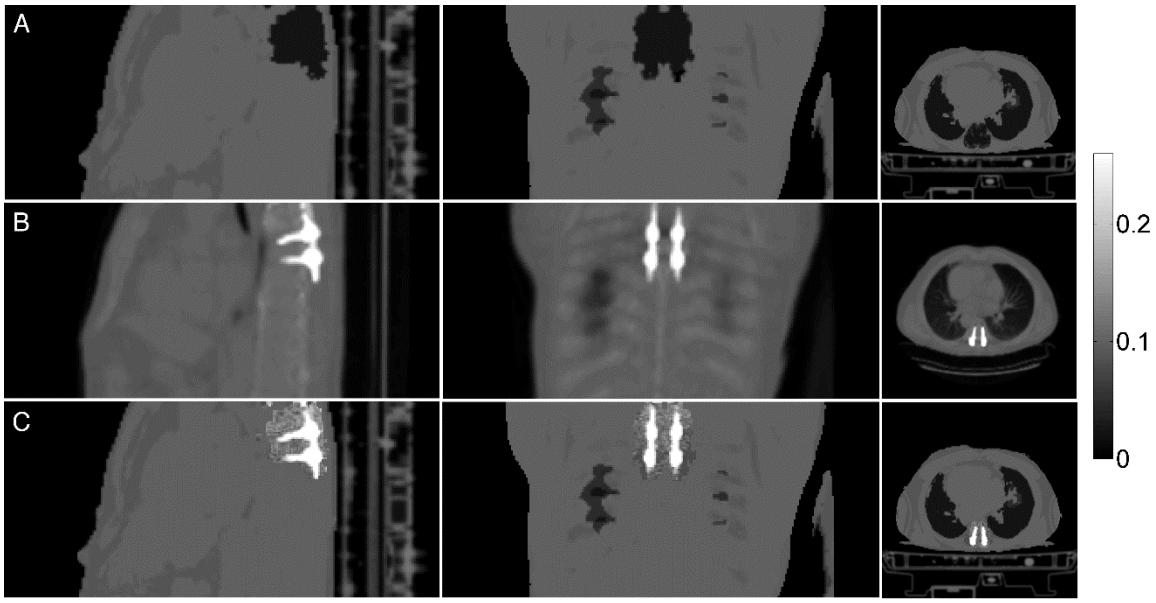

Figure 3

Patient presenting titanium spinal implant and pedicle screws (Patient 1B). Dixon (A), CT (B) and IPAC (C) μ-maps are shown. The three columns show (from left to right) sagittal, coronal and axial planes.

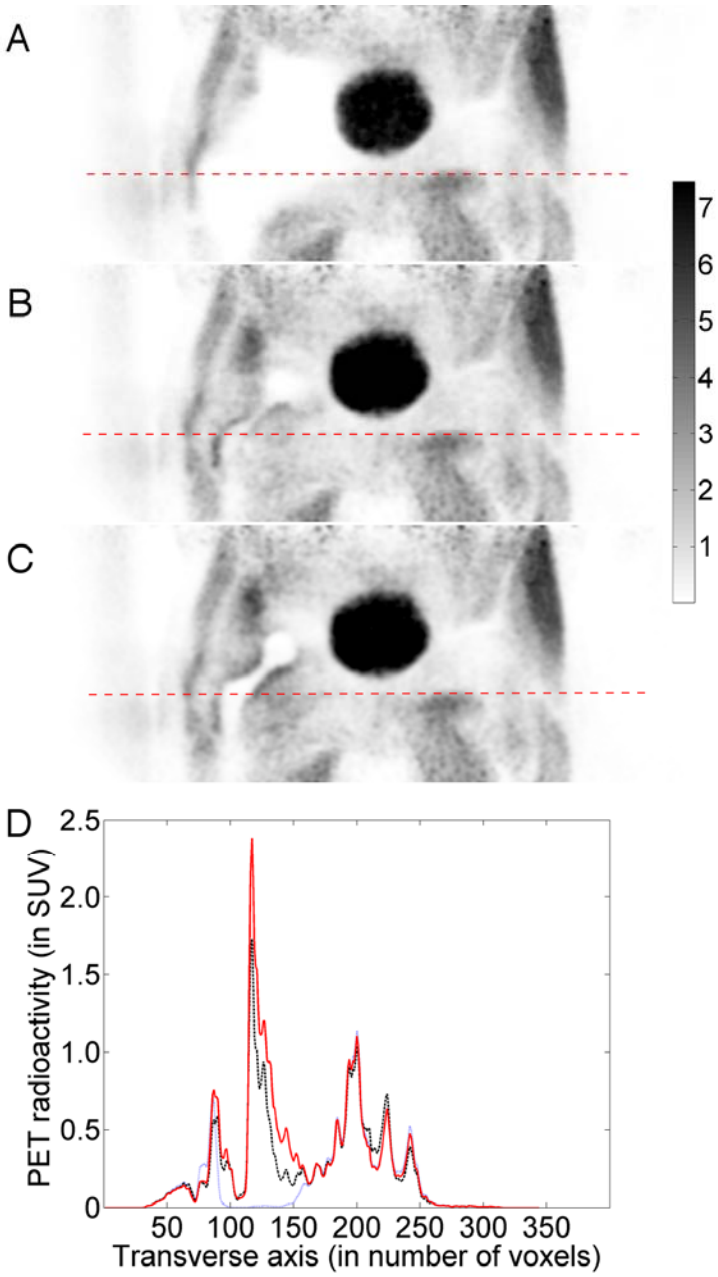

Figure 4

The reconstructed PET images corrected with the three AC methods for the validation subject of Figure 2. Dixon (A), thCT (B) and IPAC (C) μ-maps were respectively used for AC during reconstruction. The corresponding radioactivity profiles are shown in Figure D (Dixon in blue, thCT in black and IPAC in red).

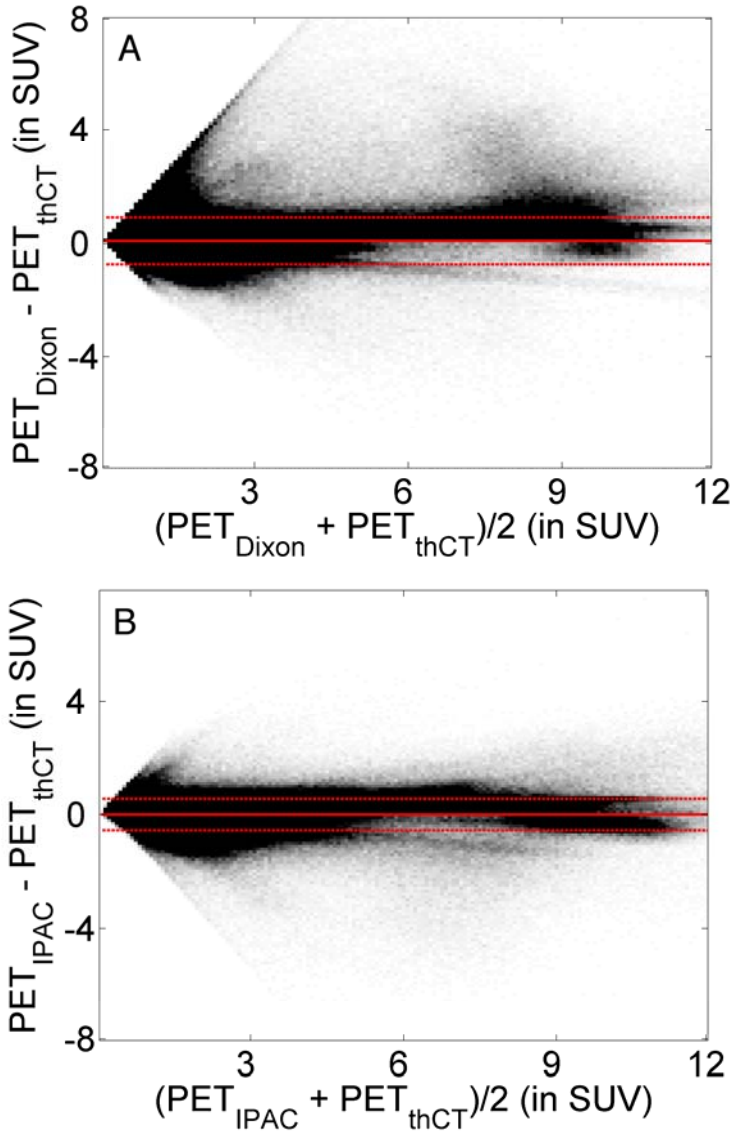

Figure 5

Bland-Altman plots showing the voxel-based comparisons (for all validation subjects) between: (A) PET_{Dixon} / PET_{thCT} and (B) PET_{IPAC} / PET_{thCT}. The continuous red lines show the mean and the dashed red lines show the standard deviation of the difference.

TABLES

Table 1: Data acquisition parameters, implant material specifications and results for DSC and mean LAC analysis.

Patient #	Center	Type of implant	Material mean LAC	Reconstructed mean LAC	DSC	Total prompts events
1	Martinos	Right hip	0.72	0.66	0.89	4.28E+08
2	SDN Napoli	Left Hip	0.36	0.32	0.80	8.55E+07
3	SDN Napoli	Both hips	0.36	0.30	0.75	4.84E+07
4	SDN Napoli	Both hips	0.36	0.31	0.75	2.70E+08
5	SDN Napoli	Right hip	0.36	0.31	0.69	2.48E+08
6	SDN Napoli	Both hips	0.36	0.28	0.69	7.50E+07
7	SDN Napoli	Both hips	0.36	0.28	0.79	3.54E+07
8	SDN Napoli	Left Femur	0.36	0.26	0.65	1.07E+08
1B	Martinos	Back Screws	0.36	0.32	0.72	2.33E+08
2B	SDN Napoli	Back Screws	0.36	0.33	0.66	1.21E+08
9	Martinos	Back Screws	0.36	0.27	0.65	2.40E+08
10	Martinos	Dental	-	0.29	0.64	1.80E+08
11	Martinos	Dental	-	0.28	0.66	1.13E+08
Phantom	Martinos	Hip	0.71	0.70	0.90	1.92E+08

Supplemental figure 1

A hip cobalt/chromium endoprosthesis placed in the center of a plastic phantom. The figure shows the phantom before it was completely filled with water mixed with ~54 MBq of ^{18}F-FDG.

Supplemental figure 2

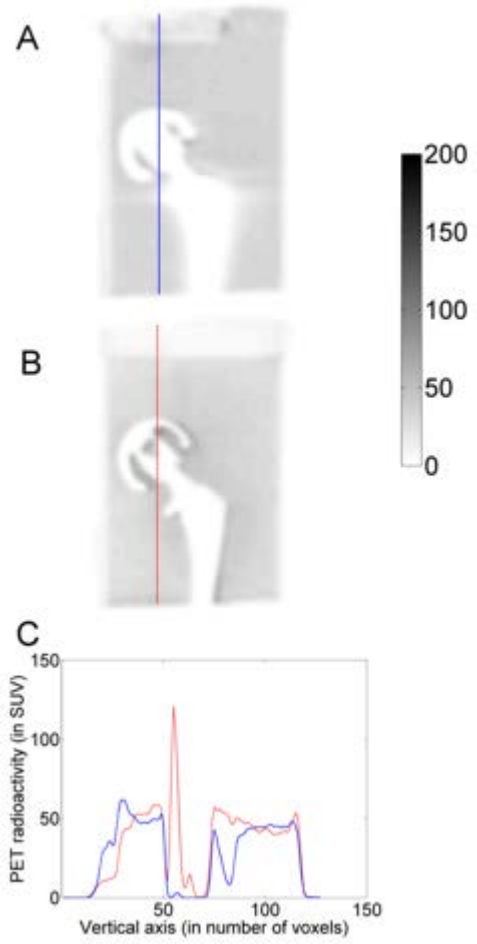

The reconstructed PET images corrected with the CT- and IPAC-based AC methods for the phantom experiment of Figure 1. CT (A) and IPAC (B) μ-maps were respectively used for AC during reconstruction. The corresponding radioactivity profiles are shown in Figure C (CT in blue and IPAC in red).

Supplemental figure 3

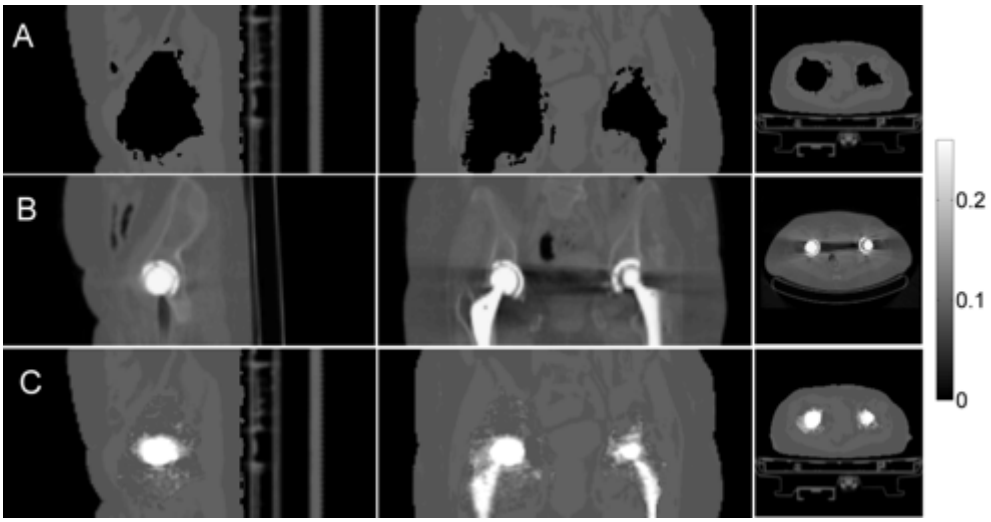

Patient presenting titanium endoprosthesis on both hips (Patient 4). Dixon (A), CT (B) and IPAC (C) μ-maps are shown. The three columns show (from left to right) sagittal, coronal and axial planes.

Supplemental figure 4

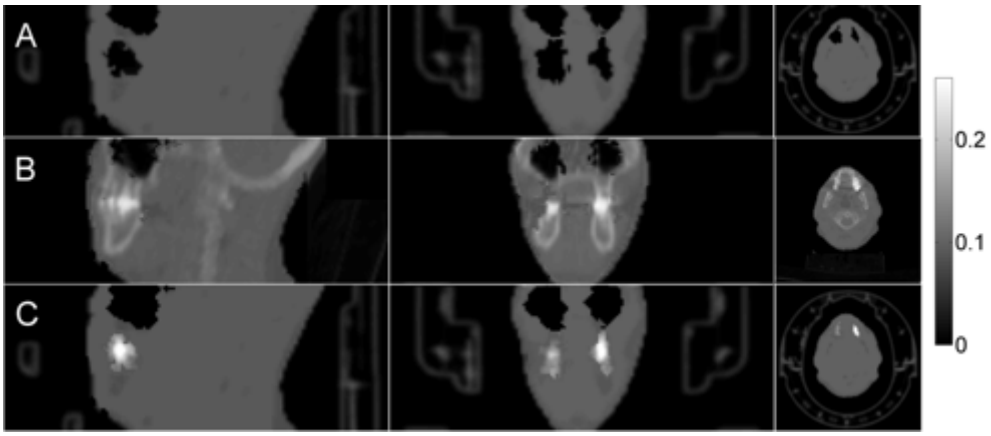

Patient presenting dental implants (Patient 10). Dixon (A), CT (B) and IPAC (C) μ-maps are shown. The three columns show (from left to right) sagittal, coronal and axial planes.

Supplemental table 1: Voxel-based analysis results on reconstructed PET images.

Patient #	Implant Volume (cm^3)	Scan duration (s)	Radiotracer activity at time of injection (Bq)	Delta Time after injection (minutes)	Patient weight (Kg)	Mean Difference (IPAC)	Mean Difference (Dixon)	aRC (IPAC)	aRC (Dixon)	R (IPAC)	R (Dixon)
1	57.86	600	7.85E+08	194	107	0.0448 (0.34)	0.2634 (1.59)	9.56 (15.68)	29.25 (30.96)	0.35	0.46
2	103.48	300	3.39E+08	182	60	-0.0056 (0.18)	0.0321 (0.45)	6.32 (8.47)	13.23 (18.64)	-0.18	0.15
3	135.08	180	3.97E+08	146	50	-0.0091 (0.12)	0.0601 (1.44)	7.33 (8.88)	49.66 (16.97)	-0.49	0.56
4	126.73	360	3.90E+08	196	75	-0.1412 (0.57)	0.0322 (1.40)	21.62 (42.40)	23.80 (32.23)	-0.10	0.41
5	38.24	360	4.05E+08	110	58	0.0183 (0.19)	0.1276 (1.01)	8.87 (9.14)	24.83 (28.42)	-0.19	0.72
6	143.19	360	3.39E+08	162	60	0.0139 (0.17)	0.0385 (0.41)	9.76 (13.18)	22.12 (28.98)	0.41	0.68
7	209.02	300	3.93E+08	346	71	0.0054 (0.20)	0.1209 (0.73)	10.58 (18.53)	30.32 (36.35)	0.02	0.43
8	29.74	360	4.21E+08	218	48	0.1733 (0.68)	0.2076 (0.86)	7.95 (7.58)	9.84 (11.41)	0.16	0.39
1B	31.02	600	7.85E+08	242	107	0.1529 (0.68)	0.1563 (0.78)	10.05 (12.19)	11.01 (12.62)	0.68	0.72
2B	52.63	360	3.39E+08	171	60	0.0769 (0.28)	0.1506 (0.57)	9.48 (10.23)	20.85 (25.62)	0.59	0.69
9	32.08	600	5.25E+08	188	85	0.0624 (0.20)	0.1188 (0.44)	9.53 (9.19)	19.04 (23.94)	0.31	0.25
10	7.54	720	8.21E+08	327	122	0.2199 (0.89)	0.2337 (0.82)	10.44 (13.15)	11.46 (15.61)	0.20	0.41
11	3.12	600	5.47E+08	182	88	0.2150 (0.24)	0.0221 (0.23)	4.13 (10.05)	4.33 (11.62)	0.34	0.32
Phantom	99.04	300	5.45E+07	28	-	-	-	-	-	-	-